

Terahertz dielectric characterisation of fibres in a time-domain spectrometer

Adam Pacewicz^{*}, Paweł Kopyt, Jerzy Cuper, Mateusz Kryszicki, Bartłomiej Salski

Institute of Radioelectronics and Multimedia Technology, Warsaw University of Technology,
Nowowiejska 15/19, 00-665 Warsaw, Poland

Article info

Article history:

Received 08 Oct. 2022

Received in revised form 01 Nov. 2022

Accepted 01 Nov. 2022

Available on-line 11 Apr. 2023

Keywords:

Terahertz spectroscopy; fibre characterisation; dielectric materials.

Abstract

An innovative measurement setup for the dielectric characterisation of fibres in a terahertz time-domain spectrometer using an HDPE elliptical lens for coupling into the fibres has been built and validated by measurements of several different types of samples. The setup is based on a commercial all fibre-coupled terahertz time-domain spectrometer. Measurements of the effective refractive index have been conducted on polypropylene-based three-dimensional printing filaments, silica glass rods, and a polytetrafluoroethylene cord of lowered density, covering the frequency range of approximately 100 GHz to 1 THz. The theoretical part of the work includes numerical calculations performed via the finite difference eigenmode method and the characteristic equations of a uniform circular dielectric waveguide for a few guided modes, from which it is clear that primarily the fundamental mode propagates along the fibre. Details on model-based phase corrections, crucial to the accurate determination of the effective refractive index of dispersive fibres, have been presented as well.

1. Introduction

The development of waveguides for the terahertz frequency range (0.1–10 THz) is an active research area. Especially, dielectric guiding structures have attracted considerable attention as THz radiation is strongly attenuated by water vapour in open structures such as metal wires. Methods of coupling such waveguides to terahertz-time-domain spectrometers (THz-TDS) and studying their propagation properties, e.g., determining the effective refractive index, have been well-documented [1–9]. A recent review paper of the progress in terahertz fibres should also be noted [10]. There is also growing interest in improving dielectric characterisation methods at sub-THz frequencies [11]. The coupling methods discussed in the literature include direct illumination with the THz-TDS beam [1], which is viable when dealing with large-core fibres, parabolic mirrors [5], hyper-spherical lens [2], or symmetric-pass lens [6]. However, to the best of the authors' knowledge, a setup using an elliptical lens has not

yet been reported before, and filling this gap is the goal of this paper. The main advantage of the setup over others is the ease of alignment, as the elliptical lens acts as a support and aid in aligning the ends of the fibre under test with the optical axis. The second purpose of the paper is to provide details of a raw THz-TDS result post-processing for the unambiguous effective refractive index determination of dispersive structures. The post-processing includes solving characteristic equations of a uniform circular dielectric waveguide. It is shown that model-based phase corrections are crucial to the accurate determination of the effective refractive index of dispersive fibres.

The organization of the paper is described as follows. In section 2, fundamental dispersion relations for a uniform circular dielectric waveguide are summarized. The experimental setup and design of the elliptical lens are described in section 3. In the following section, the fibre measurement procedure, and the extraction of the effective refractive index are discussed in detail. In section 5, the measurements and computation results are provided, followed by a discussion of their validity and conclusions.

^{*}Corresponding author at: adam.pacewicz@pw.edu.pl

2. Fundamental dispersion relations for a circular dielectric waveguide

Dielectric fibres support multiple propagating modes [12]. The fundamental mode of propagation is the HE₁₁ mode, which interestingly does not exhibit a cut-off frequency [13]. Mode effective refractive indices can be calculated numerically from dispersion relations (also known as characteristic equations), the most relevant of which will be described in this section to provide a theoretical background for comparisons with the experimental results presented in the paper.

The dispersion relation for the HE₁₁ mode of a uniform circular dielectric waveguide surrounded by air is given by [12]

$$\left[\frac{J'_n(p_1 a)}{p_1 J_n(p_1 a)} + \frac{K'_n(q_2 a)}{q_2 K_n(q_2 a)} \right] \left[\frac{k_1^2 J'_n(p_1 a)}{p_1 J_n(p_1 a)} + \frac{k_2^2 K'_n(q_2 a)}{q_2 K_n(q_2 a)} \right] = \left(\frac{\beta n}{a} \right)^2 (p_1^{-2} + q_2^{-2})^2, \quad (1)$$

where n is the first mode index denoting the number of cyclical variations with the azimuthal coordinates, as well as the order of the Bessel functions, J_n (K_n) is the Bessel function of the first kind (modified Bessel function of the second kind) and order n , J'_n and K'_n are their derivatives, a is the radius of the fibre, k_1 and k_2 are the propagation constants inside and outside the waveguide which are given by

$$k_1 = \omega \sqrt{\mu_0 \epsilon_0 n_{mat}}, \quad (2)$$

$$k_2 = \omega \sqrt{\mu_0 \epsilon_0}, \quad (3)$$

where ω is the angular frequency and ϵ_0 (μ_0) is the vacuum permittivity (permeability), and n_{mat} is the index of refraction of the waveguide material. The symbol β in (1) is the mode longitudinal propagation constant, which is related to the mode effective refractive index n_{eff} by

$$\beta = \omega n_{eff} \sqrt{\mu_0 \epsilon_0}. \quad (4)$$

The symbols p_1 and q_2 in (1) are the transverse propagation constants inside and outside the waveguide, respectively

$$p_1 = \sqrt{\omega^2 \mu_0 \epsilon_0 n_{mat}^2 - \beta^2}, \quad (5)$$

$$q_2 = \sqrt{\beta^2 - \omega^2 \mu_0 \epsilon_0}. \quad (6)$$

For the mode index $n = 0$, (1) decouples into two distinct dispersion relations, namely

$$\frac{J'_0(p_1 a)}{p_1 J_0(p_1 a)} + \frac{K'_0(q_2 a)}{q_2 K_0(q_2 a)} = 0 \quad (7)$$

for TE_{0m} modes and

$$\frac{k_1^2 J'_0(p_1 a)}{p_1 J_0(p_1 a)} + \frac{k_2^2 K'_0(q_2 a)}{q_2 K_0(q_2 a)} = 0 \quad (8)$$

for TM_{0m} modes, with m denoting the root number.

The cut-off frequency for TE₀₁ and TM₀₁ modes, which determines the single-mode operation band is given by

$$f_{cutoff} = \frac{2.405 c}{2\pi a n_{mat}}, \quad (9)$$

where c is the speed of an electromagnetic wave in vacuum. Exemplary plots of the effective refractive indices of HE₁₁, TE₀₁, and TM₀₁ modes for a dielectric fibre of $a = 1$ mm, $n_{mat} = 2$ surrounded by air are shown in Fig. 1.

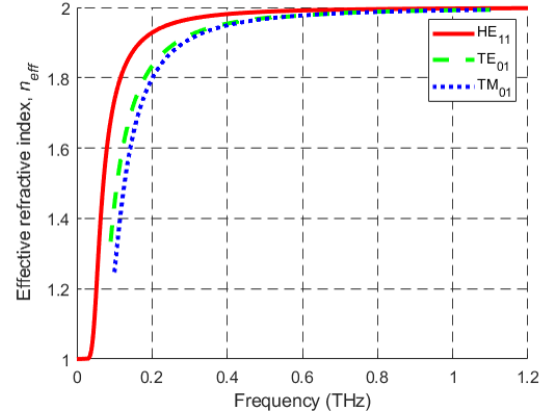


Fig. 1. Exemplary frequency dependence of the effective refractive index n_{eff} for HE₁₁, TE₀₁ and TM₀₁ modes of a dielectric fibre with the material refractive index $n_{mat} = 2$ surrounded by air and the radius $a = 1$ mm.

3. Experimental setup

3.1. Overview

The built experimental setup is shown in Fig. 2. It uses a Tera K15 all fibre-coupled terahertz time-domain spectrometer with a long scan range of 1600 ps [14]. The path of the beam is as follows. The divergent beam from the emitter E is focused onto a plane wave by a 50 mm focal-length plano-convex aspheric lens L1 made of polymethyl pentene (PMP) polymer [14]. Lens L2 is an in-house-developed high-density polyethylene (HDPE) elliptical lens with a hole enabling the placement of the fibre F at its primary focal point. The absorber A blocks any radiation that does not couple with the fibre and acts as an additional support. Lenses L2' and L1', which are the counterparts of lenses L2 and L1, couple the fibre output to the detector D.

3.2. Elliptical lens design

The design of the elliptical lens, the cross-section of which is shown in Fig. 3, proceeded as follows. Polymers

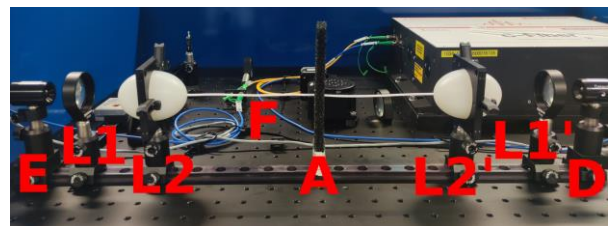


Fig. 2. Photo of the built experimental setup. E – emitter; L1, L1' – aspheric polymethyl pentene (PMP) collimating lenses, L2, L2' – elliptical collimating lenses, F – silica glass rod, A – 10 mm thick absorber, D – detector.

such as PMP are widely used in terahertz systems due to their high transparency at (sub-)THz frequencies. However, for this work, high-density polyethylene (HDPE) was chosen as it is more readily available and nearly as transparent as PMP (see Fig. 11 in Ref. 14). The permittivity of HDPE in the 0.1–1 THz range is virtually non-dispersive and amounts to $\epsilon \approx 2.33$ (refractive index $n_{mat} \approx 1.53$), which was determined as part of this work via measurements of a disk-shaped sample. The initial design parameter was the height of the lens (equal to two lengths of the semi-minor axis, a), which was fixed to 2 in (50.8 mm), where the diameter of the TPX lens (L1 and L1') was ca. 1.5 in (38.1 mm). A height of 2 in was chosen (instead of 1.5 in), so that the beam would not overlap the lens surface at high incidence angles. The length of the lens semi-major axis, b , was found via the equation [15]

$$b = \frac{a}{\sqrt{1 - \frac{1}{n_{mat}^2}}} \quad (10)$$

As per the design, the length of the semi-major (minor) lens axis is 33.615 mm (25.4 mm). This puts the two foci of the lens at 22 mm from the geometric centre of the lens. The depth of the holes for insertion of the fibre is 9.6 mm, so that the plane of contact between the fibre and lens is located 2 mm from the focal point. The depth of the hole in the lens can be increased in further studies aimed at optimizing the coupling between the fibre and the lens.

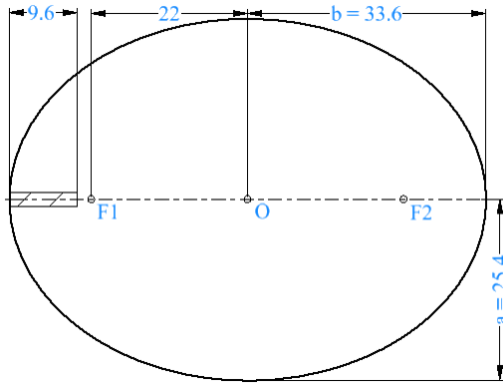


Fig. 3. Geometry of the designed and fabricated elliptical lens. The hatched area corresponds to the hole for inserting the fibre. O – centre of the lens, F1, F2 – focal points. All dimensions are given in mm.

4. Measurement and post-processing procedures

Electric field amplitude time traces of pulses transmitted through fibres of several different lengths were recorded with a constant step of $33\frac{1}{3}$ fs. Pulses resulting from secondary reflections were either insignificant or well-separated from the main pulse, which passes once through all components of the optical path. Whenever an appreciable signal background slope was present, it was recorded by taking a measurement with the emitter pulse blocked and subtracted from the measured trace. All time traces were additionally post-processed using the Tukey window with the cosine fraction $r=0.1$ before their Fourier spectra $\tilde{E}(\omega)$ were computed. To obtain a single spectrum of the

refractive index $n(\omega)$ and the absorption coefficient $\alpha(\omega)$, it is necessary to obtain the spectrum $\tilde{E}_{sam}(\omega)$ of a sample of length L_{sam} and the reference spectrum $\tilde{E}_{ref}(\omega)$ of a sample of length of $L_{ref} < L_{sam}$. Assuming that the absorption is not significant, the optical constants $n(\omega)$ and $\alpha(\omega)$ are related to the complex transmission function

$$T = \frac{\tilde{E}_{sam}(\omega)}{\tilde{E}_{ref}(\omega)} = |T| \exp(i\Delta\phi) \quad (11)$$

by the formulae [13]

$$n(\omega) = 1 + \frac{c\Delta\phi}{\omega\Delta L}, \quad (12)$$

where $\Delta L = L_{sam} - L_{ref}$ and c is the speed of an electromagnetic wave in vacuum, and

$$\alpha(\omega) = -\frac{2}{\Delta L} \ln \left[\frac{(n+1)^2}{4n} |T| \right]. \quad (13)$$

The absorption coefficient α in (13) is related to the imaginary refractive index k ($\tilde{n} = n + ik$) by [16]

$$k = \frac{\alpha c}{2\omega}. \quad (14)$$

Three kinds of materials were characterized in the built setup: Teflon (PTFE) cord, silica glass rods, and white polypropylene (PP)-based three-dimensional (3D) printing filament. The PTFE and PP samples were measured via the so-called cutback method, i.e., each fibre was successively shortened and re-measured. Measured sample lengths and diameters are summarized in Table 1. The optical constants were determined for each pair $[\tilde{E}_{sam}(\omega), \tilde{E}_{ref}(\omega)]$ of spectra corresponding to fibres of the same material but of different lengths, i.e., each sample measurement served as a reference measurement for all samples of higher length. The method is based on the assumption that the coupling coefficients between the lens and fibre remain unchanged for the different sample lengths.

Table 1
Sample dimensions.

Material	Diameter (mm)	Lengths measured (mm)
PTFE	2	282, 251.5, 220.9, 189.4, 157, 127, 97, 67.5
Silica glass	2	90, 70, 50, 30
PP	1.75	116.1, 101.1, 70.2, 55.6, 40, 28.1

The correct determination of the refractive index of dispersive structures requires careful reconstruction of the optical phase [17]. The experimental optical phase $\Delta\phi$ recovered via (11) is limited to the $[0, 2\pi]$ range. Before it can be used in (12), phase unwrapping is applied to map it to a continuous range of values, after which it should extrapolate to zero at low frequencies [17]. However, in practice, the phase in the low frequency range is scrambled due to instrumental noise. This is especially relevant for the measurement scheme that was chosen as two sample transmission spectra are available. Consequently, $\Delta\phi(f)$ is offset by an unknown number of multiples of 2π , although,

in general, the offset can be an odd multiple of π because the unwrapped phase can take a value of $\pm\pi$ at zero frequency, assuming π is the threshold value for the unwrapping algorithm. For non-dispersive materials, it follows from (11) that $\Delta\phi$ varies linearly with frequency. Thus, the constant phase offset, later denoted as ϕ_0 , can be easily determined through linear regression and subsequently subtracted from $\Delta\phi$. As will be demonstrated in the following section, for significantly dispersive materials, this method is not sufficient. However, by modelling $\Delta\phi$, for example via characteristic equations, the correct phase offset can be determined.

Equation (12) can be reformulated and the refractive index- and frequency-dependent optical phase $\Delta\phi(n, f)$ can be expressed as

$$\Delta\phi(n, f) = (n - 1) \frac{2\pi\Delta L}{c} f. \quad (15)$$

The plot of $\Delta\phi(f)$ appears as a straight line even though n may change significantly (e.g., by tens of percent). The influence of changes in n on $\Delta\phi$ is much more pronounced if the spectral deviation of n_{eff} from n_{mat} (compare Fig. 4), i.e., the quantity $\Delta\phi(n_{eff}) - \Delta\phi(n_{mat})$ is analysed, where n_{mat} is assumed to vary much more slowly with frequency than n_{eff} and is therefore approximated as a constant.

Figure 4 shows the phase difference $\Delta\phi(n_{eff}) - \Delta\phi(n_{mat})$ calculated for the PTFE cords with lengths of $L_{sam} = 282$ mm and $L_{ref} = 157$ mm, artificially offset by different values of the phase offset $\phi'_0 = \{-15\pi, \dots, -11\pi\}$, together with the theoretical phase difference calculated for the HE₁₁ mode via the characteristic equation (1) assuming $n_{mat} = 1.28$. In all experimental curves shown in Fig. 4, a constant phase offset of $\phi_0 = -6\pi$ is already accounted for. The value of ϕ_0 was found via linear extrapolation of the unwrapped phase in the frequency range of 0.28 THz–0.7 THz. By comparing the experimental curves with the

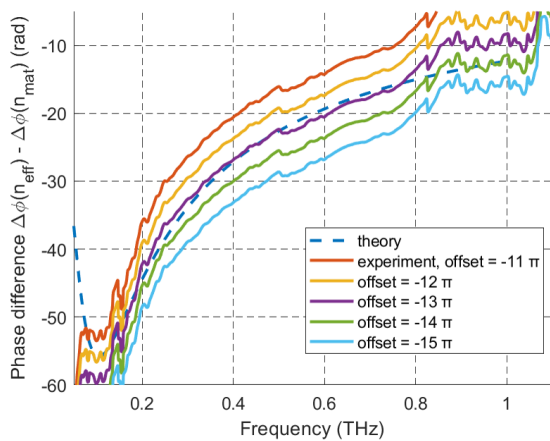


Fig. 4. Phase difference of $\Delta\phi(n_{eff}) - \Delta\phi(n_{mat})$ for PTFE measurements with $n_{mat} = 1.28$ and $L_{sam} = 282$ mm, $L_{ref} = 157$ with artificial offsets in the range of $[-15\pi, -11\pi]$ (solid lines). The quantity of $\Delta\phi(n_{eff})$ was calculated after accounting for a phase offset of $\phi_0 = -6\pi$ found via linear extrapolation. Adding an additional phase offset $\phi'_0 = -13\pi$ is necessary for the phase difference to coincide with the theoretical phase difference (dashed line) for the HE₁₁ mode computed using the characteristic equation (1).

theoretical one (which is known to extrapolate to 0 at low frequencies), the additional phase offset ϕ'_0 equal to -13π needs to be accounted for. It should be noted that neglecting ϕ'_0 results in a significant change in the value of the extracted refractive index, as shown in Fig. 5. The values of ϕ'_0 was determined for all the pairs of the measured samples and accounted for in the computation of the n_{eff} curves presented in the following section.

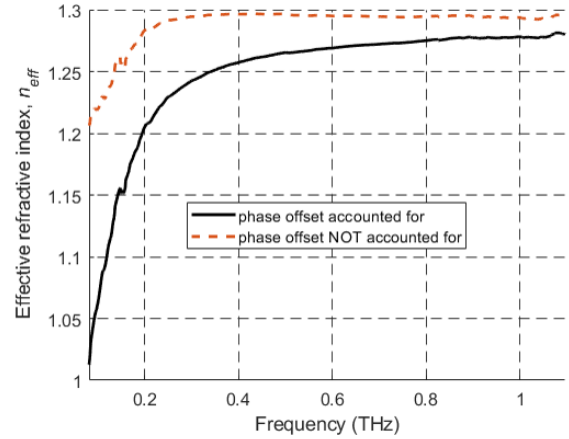


Fig. 5. Effective refractive index of the PTFE fibre computed for $L_{sam} = 282$ mm, $L_{ref} = 157$ mm with and without accounting for the additional phase offset $\phi'_0 = -13\pi$ found via comparison with the HE₁₁ mode characteristic equation (compare Fig. 4).

5. Results

The experimentally obtained frequency dependences of the effective refractive index of the PTFE cord, the PP-based 3D printing filament and silica glass rods are shown in Figs. 6–8. These results are accompanied by theoretical ones obtained via two different methods. One is the application of characteristic equations (1), (7), and (8) of the HE₁₁, TE₀₁, TM₀₁ modes, respectively, the dispersion

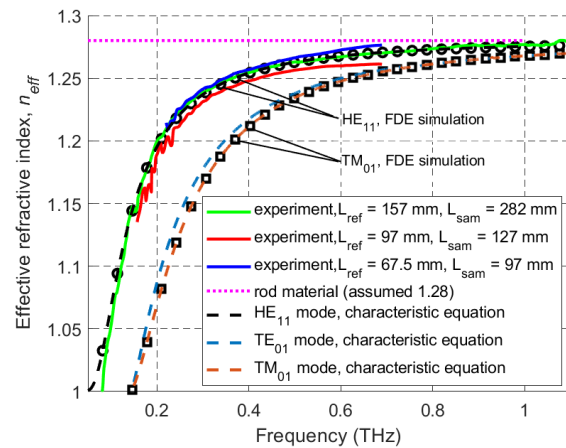


Fig. 6. Example experimental results of the effective refractive index for the porous PTFE fibre extracted from data measured for pairs of fibres of lengths of 157 mm and 282 mm, 97 mm and 127 mm, 67.5 mm, and 97 mm vs. frequency (solid lines). The dispersion relations of modes HE₁₁, TE₀₁, and TM₀₁ computed via characteristic equations (1), (7), and (8) are plotted in dashed lines. The dotted horizontal line is the material refractive index $n_{mat} = 1.28$ assumed in the computations. Empty circles and squares are results obtained via FDE computations.

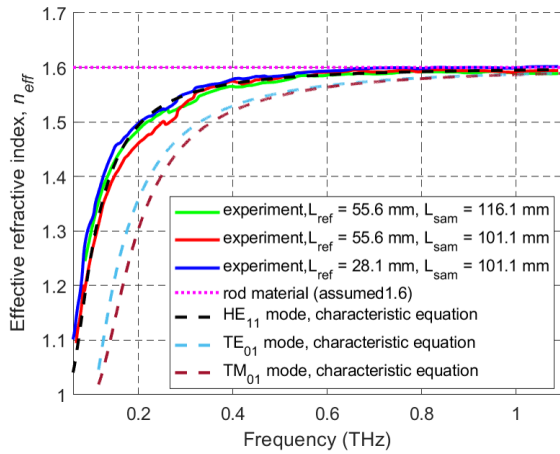


Fig. 7. Example experimental results of the effective refractive index for the PP-based 3D printing filament extracted from data measured for pairs of fibres of lengths of 55.6 mm and 116.1 mm, 55.6 mm and 101.1 mm, 28.1 mm, and 101.1 mm vs. frequency (solid lines). The dispersion relations of modes HE_{11} , TE_{11} , and TM_{01} computed via characteristic equations are plotted in dashed lines. The dotted horizontal line is the material refractive index $n_{mat} = 1.6$ assumed in the computations. Empty circles and squares are results obtained via FDE computations and pertain to the HE_{11} and TM_{01} modes, respectively.

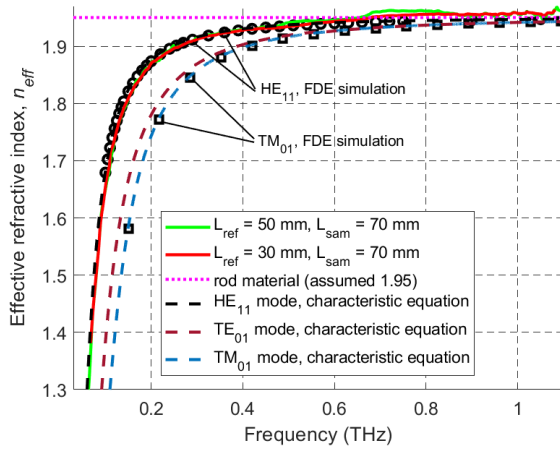


Fig. 8. Example experimental results of the effective refractive index for the silica glass rods extracted from data measured for pairs of lengths of 50 mm and 70 mm, 30 mm, and 70 mm vs. frequency (solid lines). The dispersion relations of modes HE_{11} , TE_{11} , and TM_{01} calculated via characteristic equations are plotted in dashed lines. The dotted horizontal line is the material refractive index $n_{mat} = 1.95$ assumed in the calculations. Empty circles and squares are results obtained via FDE calculations and pertain to the HE_{11} and TM_{01} modes, respectively.

relations of which are plotted with a dotted line in Figs. 6–8. The value of the material refractive index n_{mat} , which was assumed to be a constant for the characteristic equation computations, is plotted with a dotted horizontal line.

The other type of theoretical results was obtained using the finite difference eigenmode (FDE) method implemented in the Ansys Lumerical MODE solver, which can calculate a 2D cross-sectional spatial profile of modal fields, as well as the frequency dependence of the propagation constant. This method was used to compute the

effective refractive index of HE_{11} and TE_{01} modes for the PTFE and silica glass fibres only. In all computations, the fibre was assumed to be surrounded by air.

The HE_{11} modal fields of the silica glass rod at frequencies of 100 GHz, 200 GHz, and 1 THz are shown in Fig. 9. The fields significantly extend beyond the rod at 100 GHz and become increasingly confined as the frequency increases. This is reflected in the saturation of the $n_{eff}(f)$ curves to the value of n_{mat} depicted in Figs. 6–8.

The absorption coefficient (13) for the PTFE cord vs. frequency is shown in Fig. 10 alongside the absorption coefficient of bulk PTFE [18]. As it can be seen, the studied PTFE cord is clearly less lossy than its bulk counterpart (at least in the range of 0.4–1.1 THz), which will be discussed in the following section.

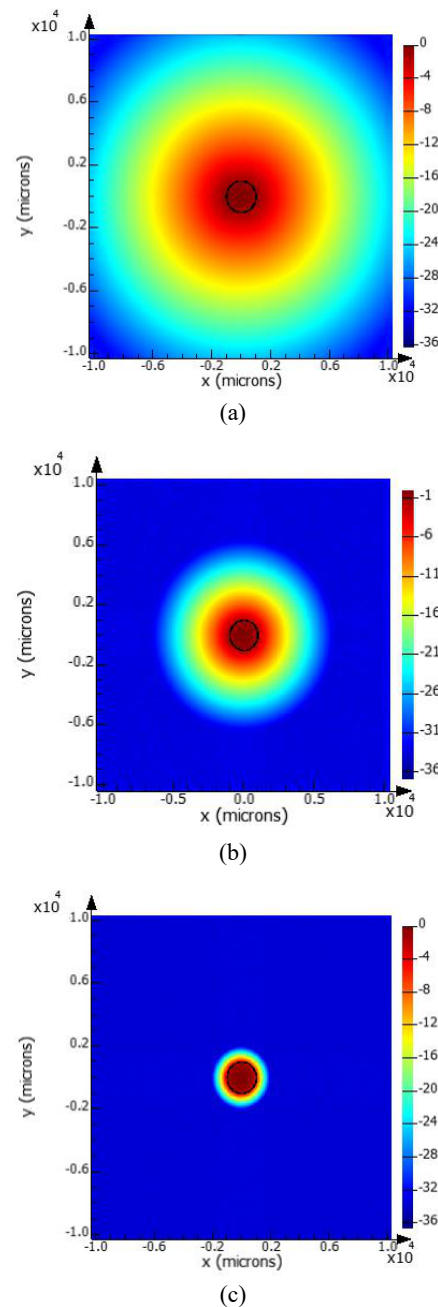


Fig. 9. Electric field intensity at 100 GHz (a), 200 GHz (b), and 1 THz (c) of the fundamental HE_{11} mode in a cross-section of a silica glass rod with a diameter of $d = 2$ microns and an assumed material refractive index of $n_{mat} = 1.95$ calculated using the Ansys Lumerical FDE solver.

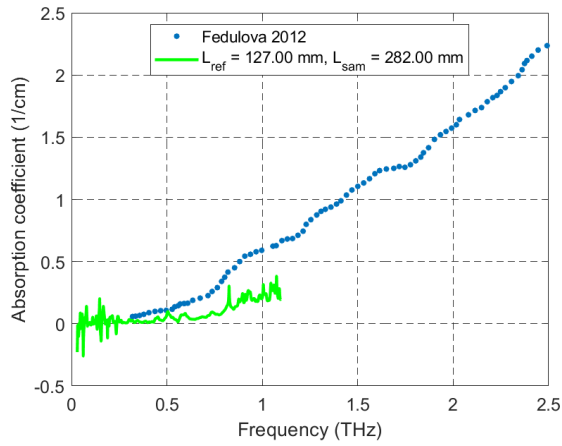


Fig. 10. Spectrum of the absorption coefficient (13) of the PTFE cord plotted alongside the absorption coefficient of bulk PTFE [18].

6. Discussion

Comparisons of the extracted effective refractive index spectra $n(\omega)$ with the theoretical dispersion relations shown in Figs. 6–8 allow to conclude that essentially fundamental mode propagation occurred in all studied materials, with the caveat that multimode propagation at higher frequencies cannot be ruled out, since the effective refractive indices of modes TE₀₁, TM₀₁ (and other higher-order ones) become close to n_{eff} of the HE₁₁ mode. Consequently, in all cases, the waveguide dispersion increases rapidly with decreasing frequency as the modal fields become less and less confined within the fibre. It is well known that as the frequency decreases, the mode area of the guided wave increases (see also Fig. 9), and the effective refractive index of the guided wave tends to the refractive index of the fibre cladding [19], which is air for the studied samples. What is more, the assumption of the constant n_{mat} turned out to be sufficient to model the experimentally determined n_{eff} via the characteristic equation (1). However, the agreement of the results with theory is visibly better for the silica rods than for the two plastic fibres, which could be attributed to the poorer sample quality (bending, inhomogeneity, diameter variations) or possibly the higher material dispersion.

For the fused silica rods, the extracted material refractive index value of $n_{mat} = 1.95$ is in very good agreement with the literature [20]. However, for the PP-based filament, the value of $n_{mat} = 1.6$ is higher than literature values for PP [21, 22] ($n_{mat} = 1.49$). This discrepancy suggests that the studied material was not pure PP but contained additives. This was partially confirmed by the separation of two phases of different density and colour observed during heating the PP filament up to 265 °C. Also, the fibre bending increases the effective refractive index [23], which may theoretically lead to an overestimation of n_{mat} , however, it was kept at a minimum in the experiments and it was assessed that its influence on n_{mat} was negligible.

With regard to the PTFE fibre, n_{mat} is equal to 1.28, which may at first be surprising since all known solid (i.e., free of air pores) materials have $n > 1.41$ at microwave and terahertz frequencies. However, the studied fibre appeared to be solid (no air pores were visible) even under micro-

scope inspection with a magnification of about 300. This fact can be explained if it is assumed that the material is in fact expanded PTFE (ePTFE), which contains sub-micron air pores [24] which may not be discernible assuming a human eye resolution of 250 μm. Indeed, the material density quoted by the manufacturer is 1.5 g/cm³, whereas the literature density value for PTFE is in the range of 2.1–2.2 g/cm³. Assuming that the refractive index is additive on a molar fraction basis [25, 26], one can estimate $n \approx 1.31$ as described below.

Additivity of the molar refraction NV of a binary mixture on a molar fraction basis can be expressed by the equation

$$NV = N_1V_1x_1 + N_2V_2x_2, \quad (16)$$

where N is the function of the refractive index n , $V = \frac{M}{\rho}$ is the molar volume, x is the mole fraction of the component i , M is the molar mass, and ρ is the density. Assuming the linear mixing rule $V = x_1V_1 + x_2V_2$ and $x_1 + x_2 = 1$, N can be determined if densities, molar masses, and refractive indices of the components are known. According to the simplest mixing rule of Arago-Biot, $N = n$ [26], thus taking $\rho_{PTFE} = 2.15$ g/cm³, $M_{PTFE} = 100.016$ g/mol [27], $n_{PTFE} = 1.43$ [18], $n_{air} = 1$, $\rho_{air} = 1.225 \times 10^{-3}$ g/cm³, $M_{air} = 28.97$ g/mol, one arrives at $n = 1.31$, which is only 2.7% higher than the value of 1.28 obtained via the characteristic equation modelling (see Fig. 6).

An additional indication of the existence of air pores is the fact that the measured absorption coefficient (see Fig. 10) is significantly lower than that of bulk PTFE.

The supporting absorber (denoted A in Fig. 2) negligibly affected the transmitted pulse, as it can be seen in the example time traces shown in Fig. 11. The absorption of radiation that did not couple to the fibre somewhat decreases the ripples in the time-domain, and, presumably, the absorber can be forgone completely, if this is tolerated. The ripples on the trailing edge of the main pulse in Fig. 11 may be attributable to a secondary reflection from the TPX lens, as each pass introduces a delay of only approximately 23 ps. Secondary reflections from the HDPE lens can be ruled out since it has been experimentally determined that a single pass through a full lens (i.e., one without the hole for the fibre) introduces a delay of as much as 136 ps.

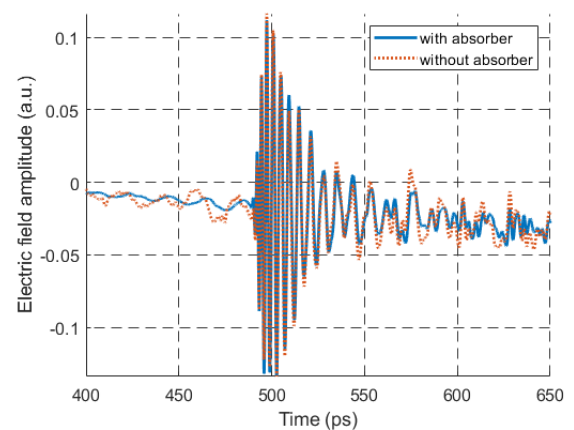


Fig. 11. Comparison of time-domain pulse traces transmitted through the setup shown in Fig. 2 with a 90 mm length silica glass rod sample, with (solid line) and without (dotted line) the absorber.

A final comment should also be made on the possible influence of diffractive limits on the results. At 100 GHz, the Abbe diffraction limit is slightly below 3 mm, which is higher than the diameter of the fibres (1.75 mm and 2 mm). This causes a large fraction of the focused beam not to couple into the fibre. In theory, this will not significantly influence the measured effective refractive index and absorption coefficient if the coupling coefficient is similar for different fibre lengths. In practice, however, the diffractive limit is likely to have made the repeatability of the coupling at low frequencies to deteriorate. This may explain the variability of the transmission spectra at low frequencies which in some cases made it impossible to extract the effective refractive index even though it was possible for longer fibres (see Fig. 6). Additionally, to rule out the possibility that the uncoupled radiation would reach the detector, all experiments were carried out with a 10 mm thick absorber.

7. Conclusions

An innovative measurement setup for the dielectric characterisation of fibres in a THz-TDS spectrometer based on an HDPE elliptical lens has been built and validated by measurements of a few different types of fibres. Comparisons of the measured effective refractive index with numerical simulations allow to conclude that it was essentially the fundamental HE₁₁ mode that propagated through the fibre. The nature of the extracted dispersion relations was influenced primarily by waveguide dispersion.

Authors' statement

Research concept and design, A.P., P.K., and B.S.; assembly of the experimental setup A.P, J.C.; collection of experimental data, A.P.; data analysis and interpretation, A.P., M.K.; numerical modelling A.P., P.K., B.S.; writing the article, A.P., P.K.; critical revision of the article, J.C., M.K.; final approval of article, B.S.

Acknowledgements

Scientific work financed from budget funds for science in 2017–2020 as a research project under the "Diamond Grant" program, project number DI 2016 021146.

The authors would like to thank Mr. Piotr Chmielewski (Warsaw University of Technology) for manufacturing the lens.

References

- [1] Atakaramians, S. *et al.* THz porous fibers: design, fabrication and experimental characterization. *Opt. Express* **17**, 14053–14062 (2009). <https://doi.org/10.1364/oe.17.014053>
- [2] Nielsen, K. *et al.* Bendable, low-loss Topas fibers for the terahertz frequency range. *Opt. Express* **17**, 8592–8601 (2009). <https://doi.org/10.1364/oe.17.008592>
- [3] Bao, H., Nielsen, K., Rasmussen, H. K., Jepsen, P. U. & Bang, O. Fabrication and characterization of porous-core honeycomb bandgap THz fibers. *Opt. Express* **20**, 29507–29517 (2012). <https://doi.org/10.1364/OE.20.029507>
- [4] Dupuis, A., Mazhorova, A., Désévéday, F., Rozé, M. & Skorobogatiy, M. Spectral characterization of porous dielectric subwavelength THz fibers fabricated using a microstructured molding technique. *Opt. Express* **18**, 13813–13828 (2010). <https://doi.org/10.1364/OE.18.013813>
- [5] Chen, L.-J., Chen, H.-W., Kao, T.-F., Lu, J.-Y. & Sun, C.-K. Low-loss subwavelength plastic fiber for terahertz waveguiding. *Opt. Lett.* **31**, 308–310 (2006). <https://doi.org/10.1364/OL.31.000308>
- [6] Anthony, J., Leonhardt, R. & Argyros, A. Hybrid hollow core fibers with embedded wires as THz waveguides. *Opt. Express* **21**, 2903–2912 (2013). <https://doi.org/10.1364/OE.21.002903>
- [7] Peretti, R., Braud, F., Peytavit, E., Dubois, E. & Lampin, J.-F. Broadband terahertz light–matter interaction enhancement for precise spectroscopy of thin films and micro-samples. *Photonics* **5**, 11 (2018). <https://doi.org/10.3390/photonics5020011>
- [8] Ponceca, Jr., C. S. *et al.* Transmission of terahertz radiation using a microstructured polymer optical fiber. *Opt. Lett.* **33**, 902–904 (2008). <https://doi.org/10.1364/OL.33.000902>
- [9] Wu, Z., Ng, W.-R., Gehm, M. E. & Xin, H. Terahertz electromagnetic crystal waveguide fabricated by polymer jetting rapid prototyping. *Opt. Express* **19**, 3962–3972 (2011). <https://doi.org/10.1364/OE.19.003962>
- [10] Islam, M. S. *et al.* Terahertz optical fibers [Invited]. *Opt. Express* **28**, 16089–16117 (2020). <https://doi.org/10.1364/OE.389999>
- [11] Kopyt, P., Cuper, J., Czekala, P., Pacewicz, A. & Salski, B. Measurements of Electromagnetic Properties of Low-loss Dielectrics in the mm-Wave and sub-THz Bands. in *TERFEL: International Conference on Free Electrons Laser Applications in Infrared and THz Studies of New States of Matter* (2022).
- [12] Yeh, C., Shimabukuro, F. *The Essence of Dielectric Waveguides*. (Springer, 2010).
- [13] Elsasser, W. M. Attenuation in a dielectric circular rod. *J. Appl. Phys.* **20**, 1193–1196 (1949). <https://aip.scitation.org/doi/10.1063/1.1698307>
- [14] MenloSystems. TERA K15 All fiber-coupled Terahertz Spectro-meter. (2022). <https://www.menlosystems.com/products/thz-time-domain-solutions/terak15-terahertz-spectrometer/>
- [15] Filipovic, D. F., Gearhart, S. S. & Rebeiz, G. M. Double-slot antennas on extended hemispherical and elliptical silicon dielectric lenses. *IEEE Trans. Microw. Theory Techn.* **41**, 1738–1749 (1993). <https://doi.org/10.1109/22.247919>
- [16] Agrawal, G. P. *Nonlinear Fiber Optics-Fifth Edition. Nonlinear Fiber Optics* (Academic Press, 2013).
- [17] Jepsen, P. U. Phase retrieval in terahertz time-domain measurements: a “how to” tutorial. *J. Infrared Millim. Terahertz Waves* **40**, 395–411 (2019). <https://doi.org/10.1007/s10762-019-00578-0>
- [18] Fedulova, E. V. *et al.* Studying of dielectric properties of polymers in the terahertz frequency range. *Proc. SPIE* **8337**, 83370I (2012). <https://doi.org/10.1117/12.923855>
- [19] Han, H., Park, H., Cho, M. & Kim, J. Terahertz pulse propagation in a plastic photonic crystal fiber. *Appl. Phys. Lett.* **80**, 2634–2636 (2002). <https://doi.org/10.1063/1.1468897>
- [20] Naftaly, M. & Gregory, A. Terahertz and microwave optical properties of single-crystal quartz and vitreous silica and the behavior of the Boson peak. *Appl. Sci.* **11**, 6733 (2021). <https://doi.org/10.3390/app11156733>
- [21] Busch, S. F. *et al.* Optical properties of 3D printable plastics in the THz regime and their application for 3D printed THz optics. *J. Infrared Millim. Terahertz Waves* **35**, 993–997 (2014). <https://doi.org/10.1007/s10762-014-0113-9>
- [22] Squires, A. D. & Lewis, R. A. Feasibility and characterization of common and exotic filaments for use in 3d printed terahertz devices. *J. Infrared Millim. Terahertz Waves* **39**, 614–635 (2018). <https://doi.org/10.1007/s10762-018-0498-y>
- [23] Hadi, M., Husein, A. & Alan Deta, U. A refractive index in bent fibre optics and curved space. *J. Phys. Conf. Ser.* **1171**, 012016 (2019). <https://doi.org/10.1088/1742-6596/1171/1/012016>

- [24] Guo, Y. *et al.* A novel process for preparing expanded Polytetrafluoroethylene(ePTFE) micro-porous membrane through ePTFE/ePTFE co-stretching technique. *J. Mater. Sci.* **42**, 2081–2085 (2007).
<https://doi.org/10.1007/s10853-006-1214-1>
- [25] Pretorius, F., Focke, W. W., Androsch, R. & du Toit, E. Estimating binary liquid composition from density and refractive index measurements: A comprehensive review of mixing rules. *J. Mol. Liq.* **332**, 115893 (2021).
<https://doi.org/10.1016/j.molliq.2021.115893>
- [26] Arago, D. F. J. and Biot, J. Refractive properties of binary mixtures. *Mem. Acad. Fr.* **15**, 7–11 (1806).
- [27] Teflon. *ChemBK*. (2022).
<https://www.chembk.com/en/chem/TEFLON>